JOURNAL OF GEOPHYSICAL RESEARCH: SPACE PHYSICS, VOL. 118, 181–191, doi:10.1029/2012JA017915, 2013

Evidence for potential and inductive convection during intense geomagnetic events using normalized superposed epoch analysis

Roxanne M. Katus,[1] Michael W. Liemohn,[1] Dennis L. Gallagher,[2] Aaron Ridley,[1] and Shasha Zou[1]

Received 4 May 2012; revised 12 October 2012; accepted 12 November 2012; published 17 January 2013.

[1] The relative contribution of storm-time ring current development by convection driven by either potential or inductive electric fields has remained an unresolved question in geospace research. Studies have been published supporting each side of this debate, including views that ring current buildup is entirely one or the other. This study presents new insights into the relative roles of these storm main phase processes. We perform a superposed epoch study of 97 intense ($Dst_{Min} < -100$ nT) and 91 moderate (-50 nT $> Dst_{Min} > -100$ nT) storms using OMNI solar wind and ground-based data. Instead of using a single reference time for the superpositioning of the events, we choose four reference times and expand or contract each phase of every event to the average length of this phase, creating a normalized timeline for the superposed epoch analysis. Using the bootstrap method, we statistically demonstrate that timeline normalization results in better reproduction of average storm dynamics than conventional methods. Examination of the *Dst* reveals an inflection point in the intense storm group consistent with two-step main phase development, which is supported by results for the southward interplanetary magnetic field and various ground-based magnetic indices. This two-step main-phase process is not seen in the moderate storm timeline and data sets. It is determined that the first step of *Dst* development is due to potential convective drift, during which an initial ring current is formed. The negative feedback of this hot ion population begins to limit further ring current growth. The second step of the main phase, however, is found to be a more even mix of potential and inductive convection. It is hypothesized that this is necessary to achieve intense storm *Dst* levels because the substorm dipolarizations are effective at breaking through the negative feedback barrier of the existing inner magnetospheric hot ion pressure peak.

Citation: Katus, R. M., M. W. Liemohn, D. L. Gallagher, A. Ridley, and S. Zou (2013), Evidence for potential and inductive convection during intense geomagnetic events using normalized superposed epoch analysis, *J. Geophys. Res. Space Physics*, *118*, 181–191, doi:10.1029/2012JA017915.

1. Introduction

[2] A geomagnetic storm is usually defined by a decrease in the north-south component (H) of the terrestrial magnetic field at low to middle latitudes. These events are attributed to solar wind driven particle injection into the inner magnetosphere that causes intensification of near-Earth space currents. The hour average of four low-to-middle latitude magnetometers, approximately equally spaced in local time, is used to calculate *Dst*, the disturbance storm time index [*Sugiura and Kamei*, 1991]. This index is well correlated to solar wind parameters [e.g., *Burton et al*., 1975; *O'Brien and McPherron*, 2000] and the total energy content of the ring current [*Dessler and Parker*, 1959; *Sckopke*, 1966; *Greenspan and Hamilton*, 2000; *Turner et al*., 2001; *Liemohn and Kozyra*, 2003; *Jorgensen et al*., 2004]. Thus, *Dst* is used to describe the magnetospheric response to changes in the solar wind [*Gonzalez et al*., 1994]. Its evolution characterizes the progression of solar wind and geomagnetic activity. This relationship can be seen by considering the storm sudden commencement, which is identified by a rapid rise in *Dst* associated with a sharp increase in solar wind dynamic pressure. Furthermore, a large southward interplanetary magnetic field (IMF) is a critical element in driving the main phase of a disturbance, which is also reflected in *Dst*.

[3] To investigate ring-current development, the 1 min resolution SYM-H index [*Iyemori*, 1990; *Iyemori et al*., 1992] is

[1]Department of Atmospheric, Oceanic and Space Sciences, University of Michigan, Ann Arbor, MI, USA.
[2]Space Science Department, Marshall Space Flight Center, Huntsville, AL, USA.

Corresponding author: R. M. Katus, Department of Atmospheric, Oceanic and Space Sciences, University of Michigan, Ann Arbor, MI, USA. (rkatus@umich.edu)

2169-9380/13/2012JA017915

sometimes used as a high-time resolution substitute for *Dst*. The time cadence of SYM-H provides critical information about physical processes that occur on time scales less than 1 h. Although the six magnetometer stations used to calculate SYM-H extend higher in latitude than those used for *Dst*, it still represents the ring current strength adequately as a *Dst* surrogate. The largest difference between SYM-H measurements at each station is used to define the ASY-H index. ASY-H is used to describe the longitudinal asymmetry of the low to middle latitude disturbance, attributed predominantly to the partial ring current [e.g., *Fukushima and Kamide*, 1973].

[4] Throughout a geomagnetic storm there are two primary methods of particle injection into the inner magnetosphere. The first transport method is the potential-driven convection. This occurs during periods of southward IMF, which allows part of the dawn-to-dusk solar wind electric field to effectively map down to the polar ionosphere. One measure of this type of convection is the cross-polar-cap-potential (CPCP). The CPCP used in this study was calculated using assimilative mapping of ionospheric electrodynamics [*Richmond and Kamide*, 1988; *Kihn and Ridley*, 2005] specified by satellites [*Reiff et al*., 1981; *Hairston et al*., 1998, 2003, 2005], ground-based radars [*Shepherd et al*., 2002; *Cousins and Shepherd*, 2010], and empirical models [*Heppner* 1977; *Sojka et al*., 1986; *Weimer* 1996; *Boyle et al*., 1997; *Weimer* 2005]. Another measure of the potential-driven convection is the polar cap (PC) index from Thule in the Northern Hemisphere or Vostok in the Southern Hemisphere [*Troshichev et al*., 1988; *Lukianova et al*., 2002]. This index is calculated independently based on data from these single near-pole stations.

[5] The second transport process, substorm activity, is usually defined as the mechanism of particle dissipation at polar latitudes, responsible for the aurora and subsequent intensification of the westward electrojet. The westward and eastward electrojets are described by the lower (AL) and upper (AU) auroral electrojet indices, respectively [e.g., *Mayaud*, 1980]. A response in both AU and AL indicates increased potential convection, because the magnetometers both poleward and equatorward of the potential extrema respond to overhead Hall currents. Although an increase in the AL index can be due to the enhanced Hall conductance [*Kamide and Kokubun*, 1996], in this study a response in AL only is used as a measure of substorm activity. In particular, the AL index describes the westward electrojet partially closing the substorm current wedge, and implies the possibility of convection in the magnetosphere due to induced electric fields. One possible explanation for the lack of response in AU during substorms is that the westward electrojet expands both poleward and equatorward, while the eastward electrojet shifts equatorward. The magnetometer originally measuring only the eastward electrojets become strongly influenced by the westward electrojet after substorm onset; therefore, AU decreases [*Feldstein et al*., 1999; *Gjerloev et al*., 2004].

[6] The relative contribution of potential and inductive electric field driven convection resulting in the development of the storm-time ring current has remained an unresolved question in geospace research. Studies have been published supporting each side of this debate, including views that ring current buildup is entirely potential fields [*Iyemori and Rao*, 1996; *Grafe and Feldstein*, 2000; *Liemohn and Kozyra*, 2002; *Keller et al*., 2005; *Zaharia et al*., 2008] or inductive fields [*Akasofu and Chapman*, 1963; *Liu and Rostoker*, 1995; *Lemon et al*., 2004], or some mixture of the two [*Fok et al*., 1999; *Ganushkina et al*., 2001; *Clauer et al*., 2003; *Ganushkina et al*., 2005].

[7] Although the physical processes central to geomagnetic activity are fairly well understood, critical factors concerning the development, timing, and magnitude remain unclear. *Feldstein* [1992] tested a number of models that predict storm-time *Dst* and found that the most successful models required knowledge of the minimum *Dst* to improve the accuracy of the *Dst* prediction, implying a nonlinear feedback. *Cade et al*. [1995] found a strong correlation between *Dst* and a time-weighted accumulation of the AE and AL auroral electrojet indices. *Cade et al*. [1995] also found a parametric dependence of unknown origin in the relationship between *Dst* and AE. They speculate that this unidentified dependence is the reason that unique prediction functions are never found using correlations between IMF, *Dst*, and auroral indices. In fact, the nonlinear *Dst*(IMF) relationship in the model of *Pisarsky et al*. [1989] is thought to be another manifestation of this unknown mechanism.

[8] With the proper combination of solar wind data and ground-based magnetometer indices, it is possible to investigate the relative contributions of potential and inductive electric fields during geomagnetic storms. To address this unresolved question, this study first presents a robust yet automated method for identifying storms, which includes a technique for determining the various phases for each storm. We next compare conventional and normalizing methods of combining the data from all of the storms. Using the best of these superpositioning algorithms, we then compile, present, and interpret various data sets.

2. Method

2.1. Storm Selection

[9] The study of the average inner magnetospheric dynamics during storms requires an unbiased list of geomagnetic disturbances. To collect a "clean" list of storms, this study uses a relatively standard description of an isolated storm in an automated procedure that parses *Dst* ranging from 1970 to 2012. Selection of intense (moderate) events began with a broad search for all storm peaks with *Dst* less than or equal to −100 nT (–50 nT). Next the beginning of the main phase was defined as the maximum (least intense) *Dst* within the 24 h preceding the peak. Then the end of the recovery phase was determined by locating the maximum *Dst* within 96 h after the peak.

[10] The storm list was reduced to ensure an initially quiescent magnetosphere by applying two requirements. The first of these rules discards coinciding events by requiring at least 48 h of separation between storm peaks. The second criteria scrutinizes the initial state of the magnetosphere by excluding events in which *Dst* drops below –50 nT (–25 nT) during the 12 h prior to the beginning of the main phase.

[11] The list of disturbances was further reduced by the requirement that each event contain a storm sudden commencement. Several studies have related the solar wind dynamic pressure and change in *Dst* to estimate the effect of the Chapman-Ferraro currents on the magnetopause [e.g., *Burton et al*., 1975; *O'Brien and McPherron*, 2000]. This study approximates the existence of a storm sudden

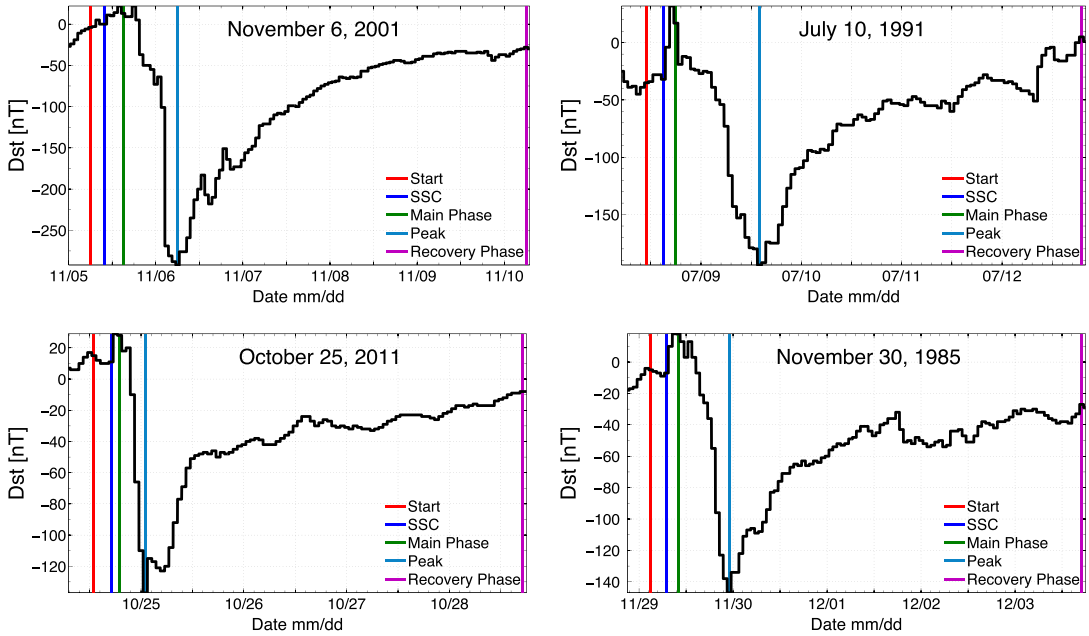

Figure 1. *Dst* for four example events found using the automated procedure described in section 2.1. Each phase is divided by vertical lines, which define the location of the epoch markers for that event.

commencement by an increase in *Dst* by at least 10 nT within 8 h before the beginning of the main phase.

[12] The full selection criterion resulted in a list of 97 intense and 91 moderate geomagnetic events. The complete list of events, reference times, and Dst_{Min} values are provided as an electronic supplement. Four example storms are presented in Figure 1. In each example the markers describe the beginning and end of each phase and a line marking 4 h prior to the storm sudden commencement.

2.2. Superposed Epoch Analysis

[13] Superposed epoch analysis is commonly used to describe the most likely dynamic behavior associated with geomagnetic storms. The first and most significant step in the procedure is defining the chronology of the disturbance. Each interval is then extracted from the complete data set and superpositioned using epoch markers. Finally, averaging along the epoch timeline removes the influence of random noise revealing the typical time series for that classification of event.

[14] Due to the variable nature of geomagnetic events, several methods of superposition have been considered. A choice often used in storm analysis [c.f., *Sugiura and Chapman*, 1960] is the initiation signature in *Dst* (the storm commencement). This fiducial has the advantage that data features at storm onset are aligned and their influence on the initial storm growth is readily seen. Another technique that provides a better superposition for the peak of the storm is to time-reference the events from their *Dst* minimum [e.g., *Loewe and Prölss*, 1997]. This reference has the advantage of aligning the driver features coincident with the transition from growth to decay. *Ilie et al.* [2008] used seven different times to superposition solar wind and magnetospheric data to conclude that, although not all indices are equally sensitive, the resolution of storm features is a function of time from a marker. A third method of analysis uses multiple references in each storm to normalize the timeline [e.g., *Yokoyama and Kamide*, 1997]. This method has the advantage of placing all of the driver features on a similar timeline with respect to these critical moments during the events.

[15] This study follows the approach taken by *Yokoyama and Kamide* [1997] and applies a more rigorous definition of a geomagnetic disturbance than conventional methods to examine the average evolution of geomagnetic perturbations. Rather than applying a generic interval surrounding a single reference point, multiple markers are used to define each event. The four distinct times indicate the beginning or end of each storm phase. Then, 4 h prior to the sudden commencement are concatenated to present information concerning the initial state of the magnetosphere. The epoch markers were then used to establish the duration of each storm phase. Several descriptive statistics associated with the span of the individual phases for the 97 intense and 91 moderate events are presented in Table 1. The mean values for the initial, main, and recovery phase of intense (moderate) disturbances were found to be 3.37, 13.38, and 74.57 h (3.88, 13.22, and 64.83 h) respectively. These values are consistent with values found in previous studies [e.g., *Pulkkinen et al.*, 2007; *Ilie*

Table 1. Moderate and Intense Storm Phase Duration Descriptive Statistics

	Mean	Mode	Minimum	Maximum	Standard Deviation
Moderate Storms					
Initial Phase	3.88	3	2	8	2
Main Phase	13.22	24	2	24	7
Recovery Phase	64.83	96	10	96	26
Intense Storms					
Initial Phase	3.37	2	2	8	2
Main Phase	13.38	24	3	24	7
Recovery Phase	74.57	96	11	96	21

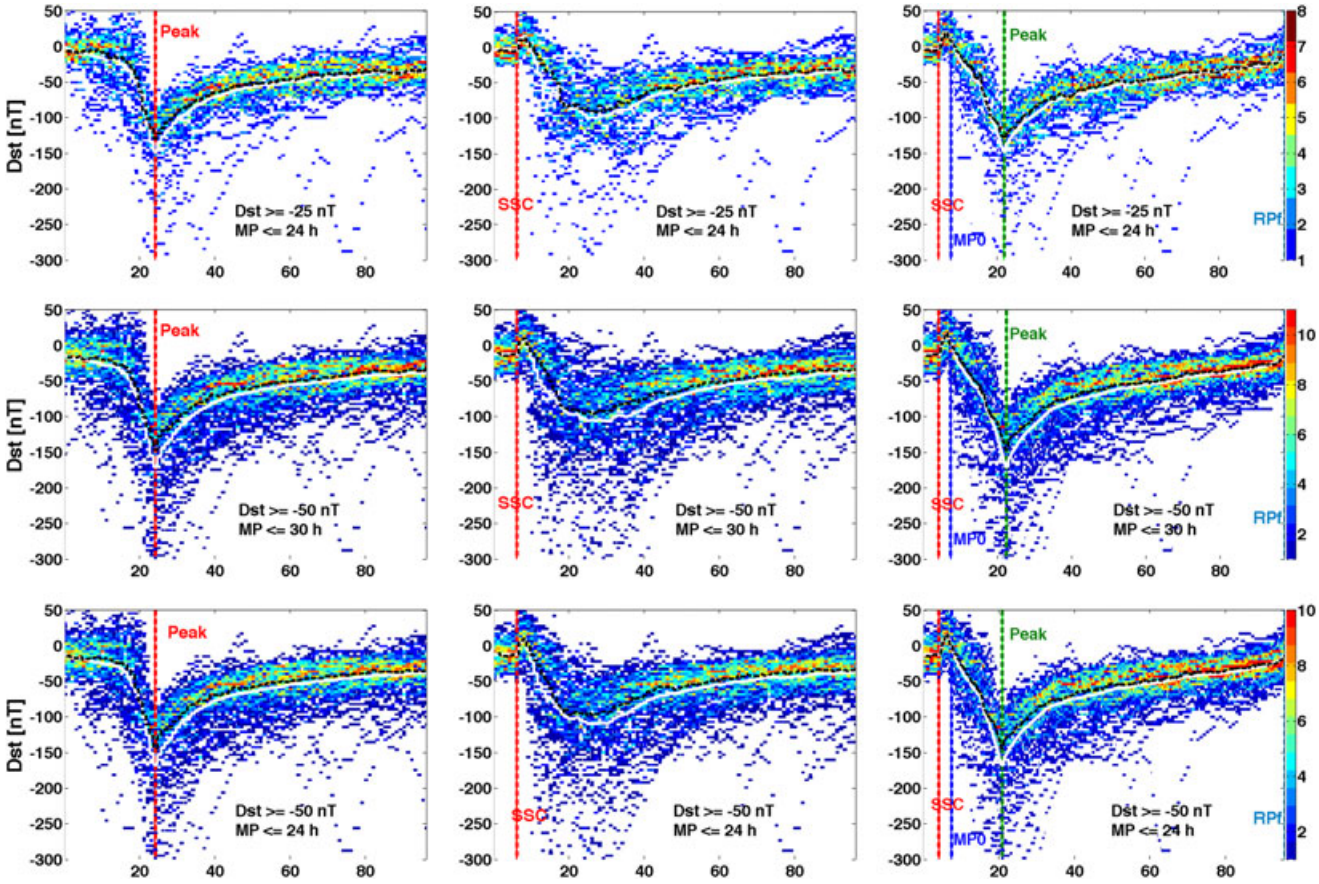

Figure 2. Superposed *Dst* for intense geomagnetic storms. The timeline is established using (left) the storm peak, (middle) the storm sudden commencement, and (right) both the beginning and end of each phase as epoch markers. The storm selection criteria are altered in each row. The color scale describes the density of data with the mean (white line) and median (black line) over-plotted.

et al., 2008]. Histograms of the phase lengths of moderate and intense events are provided as an electronic supplement.

[16] To describe typical behavior of a standard geomagnetic event, the mean duration of each storm phase was utilized to normalize the epoch timeline. The individual storm phases were essentially stretched or compressed to the corresponding average extent of each phase using linear interpolation. The transformation applied the average duration of each phase to establish the epoch timeline, then superposed the data and calculated the mean at each time step. Therefore, the normalized result should also better represent the average rate of change than conventional techniques.

2.3. Bootstrap Resampling

[17] Numerous methods exist for the analysis of superposed epoch data. This study employs the bootstrap resampling method [*Huber*, 1981; *Efron and Tibshirani*, 1993] to quantify variation in several statistical measurements. Two statistics are chosen for examination in the sections below: the linear correlation coefficient and the root-mean-square error (RMSE). Given two data sets on the same time line, a single correlation coefficient and an RMSE value can be calculated. The bootstrap algorithm produces a large number of correlation coefficients and RMSE values between individual pairs of storms. The method involves resampling of the original pairs of data N times, randomly selecting pairs of data with the allowance of replacement, so that some data are excluded while other pairs are included multiple times. From this resampling, a new correlation coefficient and RMSE value can be calculated. This procedure is repeated as many times as necessary to produce a distribution of the statistical attributes of the original data sets. In this study, the storm list was randomly resampled to create 500 combinations of events, a number that provides a robust error interpretation around the original value of the statistic [*Huber*, 1981; *Liemohn and Katus*, 2012]. The collection of each descriptive statistic calculated from the individual sample storm sets were then used to construct a relative frequency histogram, which is then fitted to produce a probability distribution.

[18] Note that the sample size of data is quite large. The time series of data considered for this analysis extends across approximately 96 h of 1 min values; so, 5760 min values for each storm (91 moderate and 97 intense events). This yields around 524,160 min of data for the moderate storms and 558,720 min for the intense storms. Because the sample size is so large, essentially any nonzero correlation coefficient is statistically significant. However, the usefulness of the bootstrapping method is that it provides an error estimate for each statistic from the data, and therefore makes it possible to conduct hypothesis testing to quantify the

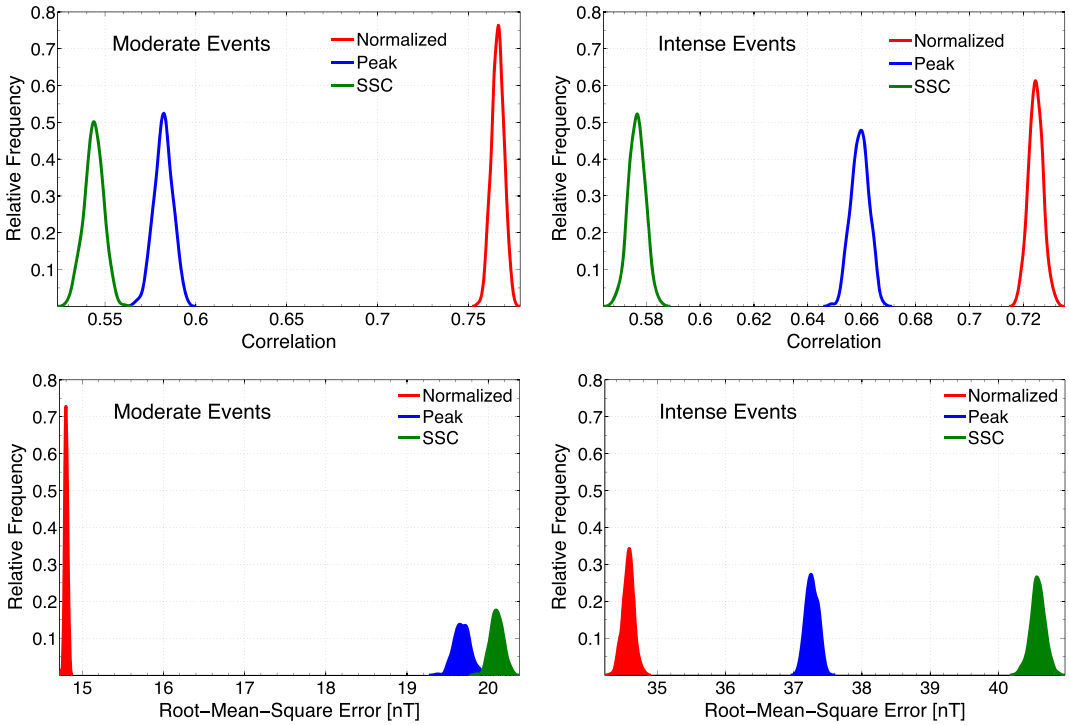

Figure 3. Distributions of the correlation coefficient between the data for each storm (top) and the root-mean-square error between the mean and corresponding superpositioned data and (bottom) for moderate (left) and intense (right) geomagnetic storms.

similarity or difference between data sets. This method will be used in section 3 to select the best superpositioning technique and reference time.

[19] Two data set creation and resampling methods are used for this study, one for the correlation coefficient and another for RMSE. This was done to verify that the findings are independent of the statistical methodology. For the correlation coefficients, the *x*-*y* pairs are created by selecting pairs of storms from the list. Therefore, entire storms are either included (perhaps several times) or excluded in the resampling. For RMSE, the approach is more traditional, with the *x* values being data from the individual storms while the corresponding *y* value is the mean (i.e., the average for the selected superposed epoch time of the *x* value datum). A bootstrap resampling is determined by randomly selecting *N* data pairs from the full list.

3. Results

3.1. Single Versus Multiple Epoch Markers

[20] The format used to present the results of the superposed epoch analysis is illustrated in the individual plots in Figure 2. The color scale describes the data density, which has been partitioned into 100 bins at each time step. The density of data points varies with storm list and data availability. Although the color scale of each plot in Figure 2 is the same, this is not always the case. The distribution of data provided by the density can be used to portray the mode and the error in the over plotted mean (white line) and median (black line). The vertical lines denote each epoch marker.

[21] The columns in Figure 2 display the *Dst* index for the intense storms, superpositioned using a 4 d interval surrounding the storm peak and sudden commencement and the normalized timeline, respectively. The sensitivity of the superposed epoch analysis to the automated storm selection criteria can be examined by comparing the rows in Figure 2. The middle row presents the results using the maximum main phase duration of 24 h and an initial main phase *Dst* closer to zero than –50 nT, which is consistent with the intense storm criteria described in section 2. The top row alters the initial *Dst* value to –25 nT while the bottom row changes the maximum duration to 30 h. Comparing the data density in the top two rows discloses that requiring a more quiescent initial state of the magnetosphere reduces the list from 97 to 55 intense events. Changing the main phase search interval increased the number of events to 102. Examining the normalized epoch timelines (right column) in the bottom two rows discloses that the extension of the maximum main phase duration results in an increase of the average from 13.38 to 14.97 h. Although these values, along with the range in peak *Dst*, slightly vary between each row, the final result is nearly identical. The findings described above are consistent with that of the moderate storms, which is not shown. The implication of this comparison is that the study outcome is insensitive to small variations in the selection criteria.

[22] The method of defining the timeline of a geomagnetic storm has a strong influence on the superposed epoch analysis. The sudden commencement is indistinguishable in any of the plots in the left column of Figure 2, when the peak *Dst* is used to delineate the event, while there is no prominent peak *Dst* in the middle column of Figure 2, when the sudden commencement is used as the reference time. Compare these with the result produced with multiple markers, the right column of Figure 2, which maintains both features. This outcome is again consistent with that of the moderate storms (not shown). Therefore, the normalized superposed epoch timeline better

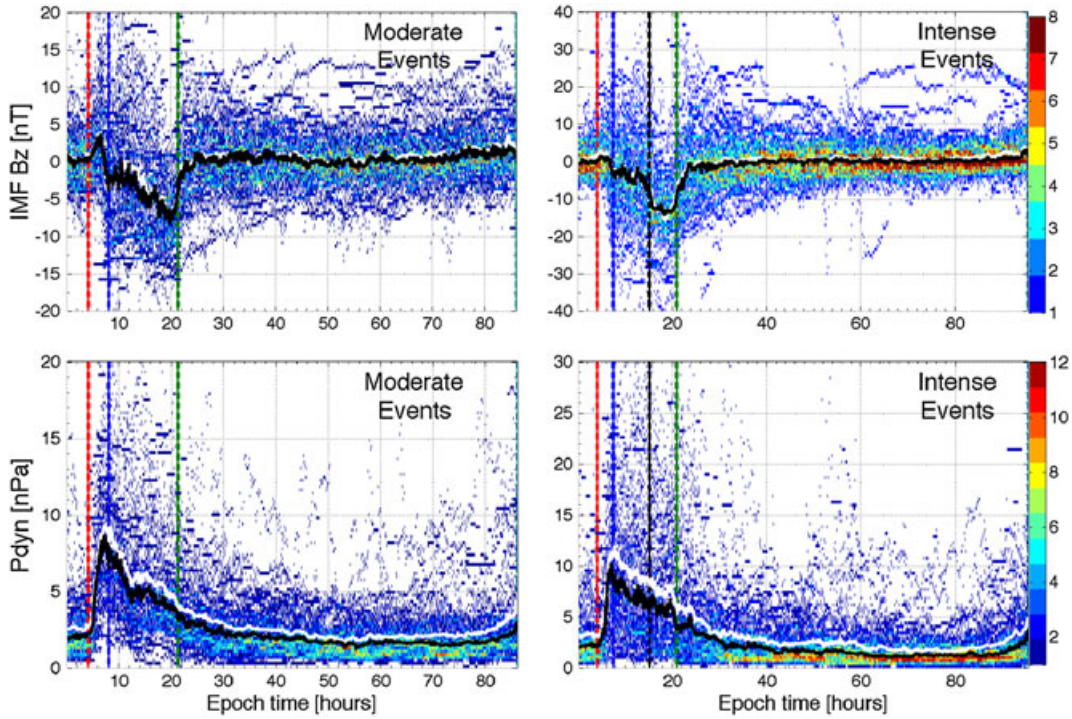

Figure 4. Superposed epoch analysis of solar wind parameters for moderate (left) and intense (right) geomagnetic storms using the normalized timeline. The color scale describes the density of data with mean (white line) and median (black line).

replicates the trend regardless of variations in the storm selection criteria for both moderate and intense storms.

[23] The outcome of a quantitative comparison of the methods of superposing the *Dst* index using the bootstrap resampling technique is presented in Figure 3. The 97 intense (left) and 91 moderate (right) storms were randomly resampled 500 times and utilized in the production of the probability distributions of correlation given in the top row of Figure 3. As a reference, the top row retains the histogram (100 bins) used to fit the distribution for correlation between each storm showing that the fitting procedure captures all of the features in the histogram. The peak value of each distribution reveals that the correlation for moderate and intense (left and right, respectively) storms is higher for the normalized timeline ($r = 0.766$ and 0.725 for moderate and intense events, respectively) than the intervals surrounding the storm sudden commencement ($r = 0.544$ and 0.712) or peak ($r = 0.582$ and 0.629). Additionally, the error between the mean and individual values along each time step was resampled 500 times to make the RMSE distributions, displayed in the bottom row of Figure 3. The peak value of each distribution reveals that the RMSE for moderate and intense (left and right) events is lower for storms superpositioned using the normalized timeline (RMSE = 14.8 and 34.58 nT) than using an interval surrounding the storm sudden commencement (RMSE = 20.1 and 40.58 nT) or peak (RMSE = 19.7 and 37.27 nT). The standard deviation of the distributions in Figure 3 can be used to make the results of hypothesis testing intuitive. The distributions for each method of creating the epoch timeline are mutually exclusive (i.e., nonoverlapping). This tells us the increased correlation and decreased RMSE for the normalized storms is statistically significant.

[24] Examining the complete set of findings presented in Figure 3 verifies that the error in the mean is lower and the storms have a higher correlation when *Dst* was superpositioned using multiple epoch markers to normalize the timeline. In addition to these results, the bootstrap distributions for several variations of the storm selection criteria and multiple geomagnetic and solar wind data sets were investigated (not shown). In practically every case, the result was consistent with those presented here for the *Dst* index. Therefore, for the remainder of this study, the normalized timeline for the superposed epoch analysis will be used.

3.2. Solar Wind Data

[25] Several additional data sets superpositioned along the normalized epoch timeline for moderate and intense storms created using *Dst* are presented in the following subsections. Some of these data sets are provided by OMNI or the Kyoto World Data Center, in both low (1 h) and high (1 min) resolution with varying ranges of availability. High-resolution data were used whenever possible but, if missing, the low-resolution data were interpolated to the high-resolution cadence to fill in as many gaps as feasible.

[26] Solar wind data superpositioned along the *Dst*-defined normalized timeline were inspected to investigate the relationship between the driver of geospace activity and the resulting magnetospheric morphology. Minimum variance, time propagated ACE, WIND, and IMP8 solar wind data [*Weimer et al.*, 2003; *Weimer*, 2004] were used to maintain the least possible time delay error. The solar wind dynamic pressure and southward IMF data for moderate and intense geomagnetic disturbances superpositioned along the normalized timeline created using *Dst* are

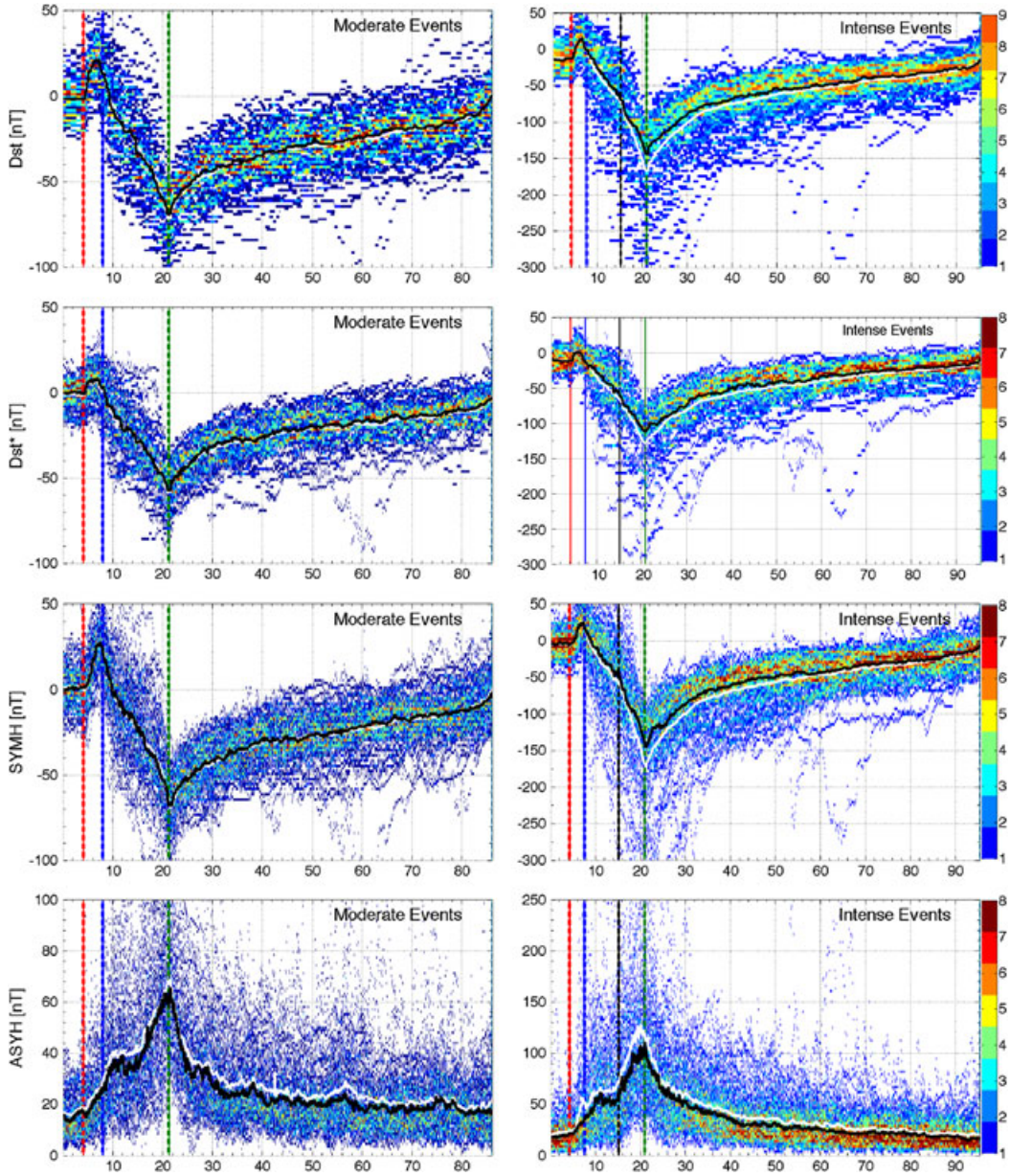

Figure 5. Superposed epoch analysis *Dst*, *Dst**, SYM-H, and ASYM-H for moderate (left) and intense (right) geomagnetic storms using the normalized timeline. The color scale describes the density of data with mean (white line) and median (black line).

presented in Figure 4. The color scale again describes data density partitioned into 100 bins along the *y*-axis, while the white line defines the mean (solid) and median (dashed) values.

[27] The results in Figure 4 are consistent with the general description of solar wind observations during a storm [*Gonzalez et al.*, 1994]. The average IMF begins with a relatively sharp change from near zero to southward at the storm sudden commencement, then drops and remains southward throughout the main phase. Additionally, the average dynamic pressure increases at the sudden storm commencement and then slowly drops below prestorm values for much of the recovery phase.

[28] There are several distinct differences between the solar wind parameters during intense (right) and moderate (left) events, presented in Figure 4. The most obvious discrepancy is the magnitude. Intense events have a larger range in data. The average southward IMF is more negative through the main phase. The average jump in dynamic pressure is sharper at the storm sudden commencement and remains larger into the recovery phase. Additional differences between intense and moderate storms arise when examining the average evolution of IMF. The average southward IMF for moderate storms decreases linearly throughout the main phase, while approximately 6 h prior to the peak (noted by the vertical black line), the intense storm average briefly progresses back toward zero.

3.3. *Dst* Variations

[29] The useful properties of *Dst* have led to multiple versions of *Dst* indices. The *Dst* index during a geomagnetic

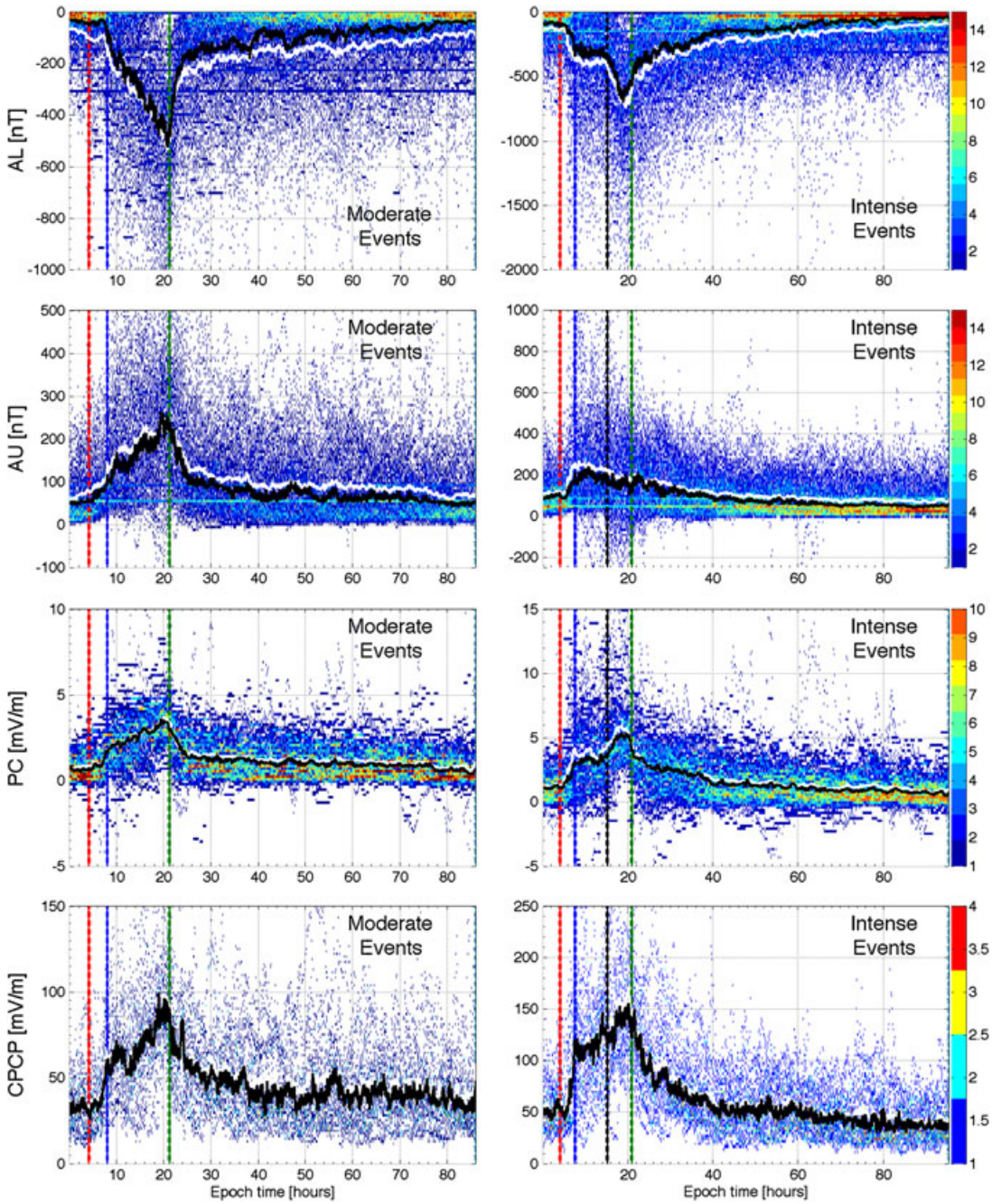

Figure 6. Superposed epoch analysis of high-latitude indices for moderate (left) and intense (right) and geomagnetic storms using the normalized timeline. The color scale describes the density of data with mean (white line) and median (black line).

storm contains magnetic perturbations originating from several current systems, such as the symmetric and asymmetric ring current, tail current, magnetopause, and ionospheric currents. By defining storm time *Dst**, the near-Earth space currents can be isolated by removing a constant offset and using a solar wind pressure correction term. Furthermore, the 1 h time cadence provided by *Dst* is often insufficient when describing physical processes that occur during disturbances. In addition, SYM-H is often used as a high resolution version of *Dst*. Measurements of the magnetic perturbation used to calculate SYM-H differ only slightly in latitude and longitude from the stations used in *Dst* observations. In addition, the largest difference between SYM-H stations, ASY-H, is often used to describe the asymmetry in the ring current. To match the 1 min solar wind data, the hourly *Dst* and *Dst** indices are interpolated to a minute cadence.

[30] Figure 5 displays the low-to-middle latitude indices (rows) superposed with normalized timelines for moderate (left) and intense (right) storms. *Dst* (top row) presents the complete storm list within the data density. Comparing *Dst* to *Dst** (second row) reveals that for both moderate and intense events, the pressure correction does not completely remove the storm sudden commencement. Examining SYM-H (third row) illustrates the increased fluctuations associated with the

higher time resolution. In each case the density of data appears to be more smoothly distributed around the mean for moderate than intense storms.

[31] The dynamics of *Dst*, *Dst**, and SYM-H all follow a consistent trend. Each of the indices increases at the storm sudden commencement and then decrease through the end of the main phase during moderate and intense events. Additionally, they all show a change in the rate of decay in the recovery phase regardless of the intensity (initially fast and very gradually slowing in recovery rate). The main difference between the two categories of intensity appears in the main phase. While each of the indices drops relatively smoothly during the main phase of the moderate storms, during intense storms their distribution spreads near an inflection point (denoted by the black vertical line) approximately 6 h prior to the peak.

[32] The variations in the ASY-H index are presented in the bottom row of Figure 5. The results are similar for moderate and intense storms. The average ASY-H rapidly increases at the storm sudden commencement. It remains nearly constant during the early main phase, then rapidly increases in the late main phase, and then drops off quickly in the early recovery phase.

3.4. Transport Processes

[33] High latitude ground-based data sets are used to describe plasma transport coupling the solar wind and the inner magnetosphere. This study used the upper (AU) and lower (AL) auroral electrojet indices along with assimilative mapping of ionospheric electrodynamics CPCP and the PC index, Thule, to examine global convection and substorm activity. The CPCP and PC indices describe the dawn-to-dusk electric field in the polar ionosphere and are used as a proxy for potential driven convection. The auroral electrojet indices describe the westward and eastward electrojets such that a response in both AU and AL indicates increased potential convection, while a response in AL only is a measure of substorm activity and the possibility of convection by induced electric fields. These parameters, superpositioned using multiple epoch markers defined by *Dst*, are presented in Figure 6. It should be noted that CPCP is only available from 1997 to 2002, while all of the others are available for nearly the full time interval from 1970 to 2011.

[34] The four plots, on the left side of Figure 6, describe moderate storms. These plots reveal that each index, on average, begins to slowly increase at the storm sudden commencement and then spikes in magnitude near the start of the main phase. The indices continue to enhance, somewhat linearly, throughout the remainder of the main phase. Then they return to prestorm values during the recovery phase. The progression of AL and AU as well as PC and CPCP indicate that the main phase of moderate storms are dominated by potential driven convection.

[35] Examination of the intense disturbances, presented in the right column of Figure 6 again reveals that each parameter is initially enhanced near the start of the main phase. However, AU then begins to return to its prestorm values while each of the other indices intensify. Both the PC and CPCP indices show a second spike in magnitude following the one seen in the southward IMF (marked by the vertical black line). This is consistent with a two-step increase in potential driven convection. Additionally, the second increase in AL and decay in AU during the main phase show that, on average, substorm activity becomes important in the second step of the main phase enhancement of intense geomagnetic events.

4. Discussion

[36] The average dynamics of moderate to intense geomagnetic disturbances were thoroughly investigated with solar wind and ground-based magnetometer data. Three methods of defining reference times within a geomagnetic event were used to create superposed epoch timelines for moderate and intense storms. Analyzing the initial results in Figure 2 revealed that key features were only maintained throughout the disturbance when the timeline was normalized. The results were quantitatively compared using the bootstrap method to create distributions with the intention of intuitively presenting the outcome of a statistical comparison. Although each data set presented in this study was examined, only the results for *Dst* are presented in Figure 3. The outcome in Figure 3 is a fair representation of the primarily repetitive conclusion for each data set. Normalizing the superposed epoch timeline produced a statistically significantly better representation of an average geomagnetic disturbance. This implies that the timeline-modified superposed epoch analysis revealed or reinforced distinctive features that are otherwise obscured by the averaging. It should be noted that this procedure assumes that the storm timeline is linearly scalable and that storm features can be compressed or expanded into an average timeline and then superposed with other storms. Smaller subgroups of the range in peak *Dst* were also examined to validate the intense storm result. Although these plots are not shown, it should be mentioned that the kink in the main phase of intense storms that divides the two-step development is present regardless of the partitioning. Note that this is similar to the finding of *Kamide et al*. [1998], who found that more than 50% of intense storms progress with a two-step main phase enhancement.

[37] Solar wind parameters for moderate and intense storms were superpositioned along the normalized epoch timeline to examine coupling and validate the automated storm selection. The results showed that the average dynamic pressure increases at the storm commencement while the average IMF becomes southward and remains southward throughout the main phase.

[38] The moderate and intense disturbances differ in both magnitude and dynamics. After the initial turn to southward Bz, the IMF appears to decrease approximately linearly during the main phase of moderate storms, but in two distinct intervals in intense disturbances. This might suggest that the magnetosphere usually requires multiple intervals of southward IMF to push *Dst* to intense storm levels.

[39] Several derivatives of *Dst* were superpositioned using multiple epoch markers for moderate and intense events and presented in Figure 5. This result illustrated the existence of two inflection points during intense disturbances. The change in the rate of *Dst* decay back toward zero during the recovery phase is consistent with ring current decay due to drift first and then charge exchange [*Liemohn et al*., 1999, 2001; *Liemohn and Kozyra*, 2003; *Liemohn and Kozyra*, 2005]. The visibility of this point in each of the average equatorial magnetic perturbation proxies further validates the enhanced resolution of the normalized method.

[40] A second inflection point appears during the main phase of intense geomagnetic events that is not distinguishable during moderate events. This means that the rate of injection into the ring current increases in two steps.

[41] Higher latitude ground-based data sets were used to describe storm-time plasma transport. The results, presented in Figure 6, were consistent with a two-step main phase enhancement of intense storms. This result confirmed the continued potential driven convection and exposed the increased importance of substorm activity during the second step of the main phase enhancement. This difference between moderate and intense storms means that, usually, enhanced substorm activity on top of strong convective driving is necessary to push an event into the intense storm category. It is hypothesized that this increase in the importance of substorms is because the preexisting hot ions, from the first step of the main phase, set up a negative feedback barrier to further injection into the inner magnetosphere. At this point, substorm dipolarizations become a necessary mechanism to overcome this obstacle, inject additional plasma into near-Earth space, and yield an intense magnetic storm. Note that this increase in substorm importance is in addition to strong potential driven convection.

[42] *Iyemori and Rao* [1996] conducted a single marker superposed epoch analysis of substorm onset during moderate to large geomagnetic storms. Aligning substorms partitioned by storm phase they showed SYM-H recovering after substorm onset. They argue that although substorms cause particle injection into the magnetospherem, they simultaneously reduce the tail current. In the present study, Figures 4 and 6 show the two-step development of IMF Bz and potential driven convection during intense storms. Under these conditions enhanced reconnection may lead to enhanced tail current countering the drop due to substorm activity. Furthermore, the timing of the substorm activity plays a critical role, allowing deeper ring current injection.

[43] There are several possibilities to further examine the lack of response in the AU index during the second half of the main phase of intense storms. Observationally, one could examine the individual stations contributing to the AU and AL indices, superposing the data by magnetic latitude and/or local time, to investigate the locations of the intensified and weakened magnetometer signals. Computationally, numerical experiments could be conducted with a global magnetospheric model (or even just an ionospheric electrodynamics model) to understand why certain places might have increased or decreased perturbation signals at certain times during magnetic storms.

5. Conclusion

[44] The relative contribution of potential and inductive convection in driving the development of a geomagnetic storm was investigated with solar wind and ground-based magnetometer data. A method of identifying moderate and intense storms in the *Dst* database was established. The list of geomagnetic disturbances found using this method was then shown to be relatively insensitive to the specific selection criteria settings. The average durations of the various phases of a storm were determined. *Dst* was then superposed using three different approaches to set up the timeline. A bootstrapping error analysis was conducted to determine the superpositioning method that best reveals the average state of the storm phases. This analysis revealed that normalizing the timeline was better than using a single reference time to conduct a superposed epoch analysis. This normalized timeline was then used to superposition each of the solar wind and ground-based indices and address the science question.

[45] Examining the results for moderate storms revealed that the magnitude of each data set jumped at the storm sudden commencement and remained elevated throughout the initial phase. During the main phase each data set continued to increase in magnitude relatively linearly. The progression of the AL and AU as well as the PC and CPCP indices implies that, on average, the buildup in the main phase of moderate storms is driven dominantly by potential convection.

[46] In addition to the difference in magnitude, intense storms show a slightly different progression through the main phase than moderate storms. During the main phase of intense events there is a distinct inflection point. This point describes a break in the driving about 6 h prior to the storm peak. Before this break, the convection indicator indices linearly increase like the moderate storm timeline. However, after this break AU steadily decreases instead of increases. This lack of response in AU, accompanied by a significant rise in AL, indicates that substorm activity becomes an important driver of storm intensification. An alternative explanation for the two-step main phase enhancement, involves a nonlinear feedback process of plasmaspheric plume material slowing reconnection at the dayside magnetopause.

[47] **Acknowledgments.** The authors would like to thank NASA and NSF for funding this research through various grants, including a NASA Graduate Student Research Program fellowship from Marshall Space Flight Center. The authors would also like to thank the Kyoto World Data Center for providing access to the *Dst*, SYMH, and *Kp* indices, and NASA's CDAWeb for providing access to the OMNI solar wind data.

References

Akasofu, S.-I., and S. Chapman (1963), Magnetic Storms: The simultaneous development of the main phase (*DR*) and of polar magnetic substorms (*DP*), *J. Geophys. Res.*, *68*(10), 3155–3158, doi:10.1029/JZ068i010p03155.

Boyle, C. B., P. H. Reiff, and M. R. Hairston (1997), Empirical polar cap potentials, *J. Geophys. Res.*, *102*(A1), 111–125, doi:10.1029/96JA01742.

Burton, R. K., R. L. McPherron, and C. T. Russell (1975), An empirical relationship between interplanetary conditions and Dst, *J. Geophys. Res.*, *80*(31), 4204–4214, doi:10.1029/JA080i031p04204.

Cade, W. B., III, J. J. Sojka, and L. Zhu (1995), A correlative comparison of the ring current and auroral electrojets using geomagnetic indices, *J. Geophys. Res.*, *100*(A1), 97–105, doi:10.1029/94JA02347.

Clauer, C. R., M. W. Liemohn, J. U. Kozyra, and M. L. Reno (2003), *The relationship of storms and substorms determined from mid-latitude ground-based magnetic maps, Disturbances in Geospace: The Storm-Substorm Relationship*, AGU Monogr. Ser., vol. 142, edited by S. J. Sharma, p. 143, AGU, Washington, D. C, doi:10.1029/GM142.

Cousins, E. D. P., and S. G. Shepherd (2010), A dynamical model of high-latitude convection derived from SuperDARN plasma drift measurements, *J. Geophys. Res.*, *115*, A12329, doi:10.1029/2010JA016017.

Dessler, A. J., and E. N. Parker (1959), Hydromagnetic Theory of Geomagnetic Storms, *J. Geophys. Res.*, *64*(12), 2239–2252, doi:10.1029/JZ064i012p02239.

Efron, B. and R. J. Tibshirani (1993), *An Introduction to the Bootstrap*, Chapman & Hall, New York.

Feldstein, Y. I. (1992), Modeling of the magnetic field of magnetospheric ring current as a function of interplanetary madium parameters, *Space Sci. Rev.*, *59*, 85.

Feldstein, Y. I., L. I. Gromova, A. Grafe, C.-I. Meng, V. V. Kalegaev, I. I. Alexeev, and Y. P. Sumaruk (1999), Auroral electrojet dynamics during magnetic storms, connection with plasma precipitation and large-scale structure of the magnetospheric magnetic field. *Ann. Geophys.*, *17*, 497–507, doi:10.1007/s00585-999-0497-3.

Fok, M.-C., T. E. Moore, and D. C. Delcourt (1999), Modeling of inner plasma sheet and ring current during substorms, *J. Geophys. Res.*, *104*(A7), 14,557–14,569, doi:10.1029/1999JA900014.

Fukushima, N., and Y. Kamide (1973), Partial ring current models for worldwide geomagnetic disturbances, *Rev. Geophys.*, *11*(4), 795–853, doi:10.1029/RG011i004p00795.

Ganushkina, N. Y., T. I. Pulkkinen, V. F. Bashkirov, D. N. Baker, and X. Li (2001), Formation of intense nose structures, *Geophys. Res. Lett.*, *28*(3), 491–494, doi:10.1029/2000GL011955.

Ganushkina, N. Y., T. I. Pulkkinen, and T. Fritz (2005), Role of substorm-associated impulsive electric fields in the ring current development during storms, *Ann. Geophys.*, *23*, 579–591, doi:10.5194/angeo-23-579-2005.

Gjerloev, J. W., R. A. Hoffman, M. M. Friel, L. A. Frank, and J. B. Sigwarth (2004), Substorm behavior of the auroral electrojet indices, *Ann. Geophys.*, *22*, 2135–2149, doi:10.5194/angeo-22-2135-2004.

Gonzalez, W. D., J. A. Joselyn, Y. Kamide, H. W. Kroehl, G. Rostoker, B. T. Tsurutani, and V. M. Vasyliunas (1994), What is a Geomagnetic Storm?, *J. Geophys. Res.*, *99*(A4), 5771–5792, doi:10.1029/93JA02867.

Grafe, A., and Y. I. Feldstein (2000), About the relationship between auroral electrojets and ring currents, *Ann. Geophys.*, *18*, 874.

Greenspan, M. E., and D. C. Hamilton (2000), A test of the Dessler-Parker-Sckopke relation during magnetic storms, *J. Geophys. Res.*, *105*(A3), 5419–5430, doi:10.1029/1999JA000284.

Hairston, M. R., R. A. Heelis, and F. J. Rich (1998), Analysis of the ionospheric cross polar cap potential drop using DMSP data during the National Space Weather Program study period, *J. Geophys. Res.*, *103*(A11), 26,337–26,347, doi:10.1029/97JA03241.

Hairston, M. R., T. W. Hill, and R. A. Heelis (2003), Observed saturation of the ionospheric polar cap potential during the 31 March 2001 storm, *Geophys. Res. Lett.*, *30*(6), 1325, doi:10.1029/2002GL015894.

Hairston, M. R., K. A. Drake, and R. Skoug (2005), Saturation of the ionospheric polar cap potential during the October–November 2003 superstorms, *J. Geophys. Res.*, *110*, A09S26, doi:10.1029/2004JA010864.

Heppner, J. P. (1977), Empirical models of high-latitude electric fields, *J. Geophys. Res.*, *82*(7), 1115–1125, doi:10.1029/JA082i007p01115.

Huber, P. J. (1981), *Robust Statistics*, John Wiley, Hoboken, N. J.

Ilie, R., M. W. Liemohn, M. F. Thomsen, J. E. Borovsky, and J. Zhang (2008), Influence of epoch time selection on the results of superposed epoch analysis using ACE and MPA data, *J. Geophys. Res.*, *113*, A00A14, doi:10.1029/2008JA013241.

Iyemori, T. (1990) Storm-time magnetospheric currents inferred from mid-latitude geomagnetic field variations, *J. Geomag. Geoelectr.*, *42*, 1249-1265.

Iyemori, T., T. Araki, T. Kamei, and M. Takeda (1992), Mid-latitude geomagnetic indices ASY and SYM (provisional) No. 1 1989, Data Analysis Center for Geomag. And Space Magnetism, Kyoto Univ., Kyoto.

Iyemori, T., and D. R. K. Rao (1996), Decay of the Dst field of geomagnetic disturbance after substorm onset and its implication to storm-substorm relation, *Ann. Geophys. 14*, 608.

Jorgensen, A. M., H. E. Spence, W. J. Hughes, and H. J. Singer (2004), A statistical study of the global structure of the ring current, *J. Geophys. Res.*, *97*, A12204, doi:10.1029/2003JA010090.

Kamide, Y., and S. Kokubun (1996), Two-component auroral electrojet: Importance for substorm studies, *J. Geophys. Res.*, *101*(A6), 13,027–13,046, doi:10.1029/96JA00142.

Kamide, Y., N. Yokoyama, W. Gonzalez, B. T. Tsurutani, I. A. Daglis, A. Brekke, and S. Masuda (1998), Two-step development of geomagnetic storms, *J. Geophys. Res.*, *103*(A4), 6917–6921, doi:10.1029/97JA03337.

Keller, K. A., M.-C. Fok, A. Narock, M. Hesse, L. Rastaetter, M. M. Kuznetsova, T. I. Gombosi, and D. L. DeZeeuw (2005), Effect of multiple substorms on the buildup of the ring current, *J. Geophys. Res.*, *110*, A08202, doi:10.1029/2004JA010747.

Kihn, E. A., and A. J. Ridley (2005), A statistical analysis of the assimilative mapping of ionospheric electrodynamics auroral specification, *J. Geophys. Res.*, *110*, A07305, doi:10.1029/2003JA010371.

Lemon, C., R. A. Wolf, T. W. Hill, S. Sazykin, R. W. Spiro, F. R. Toffoletto, J. Birn, and M. Hesse (2004), Magnetic storm ring current injection modeled with the Rice Convection Model and a self-consistent magnetic field, *Geophys. Res. Lett.*, *31*, L21801, doi:10.1029/2004GL020914.

Liemohn, M. W., J. U. Kozyra, V. K. Jordanova, G. V. Khazanov, M. F. Thomsen, and T. E. Cayton (1999), Analysis of early phase ring current recovery mechanisms during geomagnetic storms, *Geophys. Res. Lett.*, *25*, 2845.

Liemohn, M. W., J. U. Kozyra, M. F. Thomsen, J. L. Roeder, G. Lu, J. E. Borovsky, and T. E. Cayton (2001), Dominant role of the asymmetric ring current in producing the stormtime Dst*, *J. Geophys. Res.*, *106*, 10,883–10,904, doi:10.1029/2000JA000326.

Liemohn, M. W., and J. U. Kozyra (2002), *Assessing the importance of convective and inductive electric fields in forming the stormtime ring current, in Sixth International Conference on Substorms*, edited by R. M. Winglee, Univ. Washington, Seattle, p.456.

Liemohn, M. W., and J. U. Kozyra (2003), Lognormal form of the ring current energy content, *J. Atmos. Solar-Terr. Phys.*, *65*, 871.

Liemohn, M. W., and J. U. Kozyra (2005), Testing the hypothesis that charge exchange can cause a two-phase decay, in *The Inner Magnetosphere: Physics and Modeling, AGU Monogr. Ser*., vol. 155, edited by T. I. Pulkkinen, N. Tsyganenko, and R. H. W. Friedel, p. 211, Am. Geophys. Un., Washington, D. C.

Liemohn, M. W., and R. Katus (2012), Is the storm-time response of the inner magnetospheric hot ions universally similar or driver dependent?, *J. Geophys. Res.*, *117*, doi: 10.1029/2011JA017389.

Liu, W. W., and G. Rostoker (1995), Energetic ring current particles generated by recurring substorm cycles, *J. Geophys. Res.*, *100*(A11), 21,897–21,910, doi:10.1029/95JA01934.

Loewe, C. A., and G. W. Prölss (1997), Classification and mean behavior of magnetic storms, *J. Geophys. Res.*, *102*(A7), 14,209–14,213, doi:10.1029/96JA04020.

Lukianova, R., O. Troshichev, and G. Lu (2002), The polar cap magnetic activity indices in the southern (PCS) and northern (PCN) polar caps: Consistency and discrepancy, *Geophys. Res. Lett.*, *29*(18), 1879, doi:10.1029/2002GL015179.

Mayaud, P. N. (1980), *Derivation, Meaning, and Use of Geomagnetic Indices, Geophys. Monogr. Ser*., vol. 22, 154 pp., AGU, Washington, D. C., doi:10.1029/GM022.

O'Brien, T. P., and R. L. McPherron (2000), An empirical phase space analysis of ring current dynamics: Solar wind control of injection and decay, *J. Geophys. Res.*, *105*(A4), 7707–7719, doi:10.1029/1998JA000437.

Pisarsky, V. Yu., Ya. A. Feldstein, N. M. Rudenova, and A. Prigancova (1989), Ring current and interplanetary medium parameters, *Studia Geophys. Geod.*, *33*, 61, 1989.

Pulkkinen, T. I., N. Partamies, K. E. J. Huttunen, G. D. Reeves, and H. E. J. Koskinen (2007), Differences in geomagnetic storms driven by magnetic clouds and ICME sheath regions, *Geophys. Res. Lett.*, *34*, L02105, doi:10.1029/2006GL027775.

Reiff, P. H., R. W. Spiro, and T. W. Hill (1981), Dependence of polar cap potential drop on interplanetary parameters, *J. Geophys. Res.*, *86*(A9), 7639–7648, doi:10.1029/JA086iA09p07639.

Richmond, A. D., and Y. Kamide (1988), Mapping electrodynamic features of the high-latitude ionosphere from localized observations: technique, *J. Geophys. Res.*, *93*(A6), 5741–5759, doi:10.1029/JA093iA06p05741.

Sckopke, N. (1966), A general relation between the energy of trapped particles and the disturbance field near the earth, *J. Geophys. Res.*, *71*(13), 3125–3130, doi:10.1029/JZ071i013p03125.

Shepherd, S. G., et al. (2002), Cross polar cap potentials measured with Super Dual Auroral Radar Network during quasi-steady solar wind and interplanetary magnetic field conditions, *J. Geophys. Res.*, *107*, 974, doi:10.1029/2001JA000152.

Sojka, J. J., C. E. Rasmussen, and R. W. Schunk (1986), An interplanetary magnetic field dependent model of the ionospheric convection electric field, *J. Geophys. Res.*, *91*(A10), 11,281–11,290, doi:10.1029/JA091iA10p11281.

Sugiura, M., and S. Chapman (1960), The average morphology of geomagnetic storms with sudden commencement, *Abh. Akad. Wiss. Göttingen. Math. Phys. Kl.*, *4*, 1–53.

Sugiura, M., and T. Kamei (1991), Equatorial Dst Index 1957-1986, *IAGA Bulletin No.* 40, ISGI, Saint-Maur-des-fosses, France.

Troshichev, O., V. Andezen, S. Vennerstrom, and E. Friis-Cristensen (1988), Magnetic activity in the polar cap: A new index, *Planet. Space. Sci.*, *36*, 975.

Turner, N. E., D. N. Baker, T. I. Pulkkinen, J. L. Roeder, J. F. Fennell, and V. K. Jordanova (2001), Energy content in the storm time ring current, *J. Geophys. Res.*, *106*, 19,149–19,156, doi:10.1029/2000JA003025.

Weimer, D. R. (1996), A flexible, IMF dependent model of high-latitude electric potentials having "Space Weather" applications, *Geophys. Res. Lett.*, *23*(18), 2549–2552, doi:10.1029/96GL02255.

Weimer, D. R., D. M. Ober, N. C. Maynard, M. R. Collier, D. J. McComas, N. F. Ness, C. W. Smith, and J. Watermann (2003), Predicting interplanetary magnetic field (IMF) propagation delay times using the minimum variance technique, *J. Geophys. Res.*, *108*(A1), 1026, doi:10.1029/2002JA009405.

Weimer, D. R. (2004), Correction to "Predicting interplanetary magnetic field (IMF) propagation delay times using the minimum variance technique", *J. Geophys. Res.*, *97*, A12104, doi:10.1029/2004JA010691.

Weimer, D. R. (2005), Improved ionospheric electrodynamic models and application to calculating Joule heating rates, *J. Geophys. Res.*, *110*, A05306, doi:10.1029/2004JA010884.

Yokoyama, N., and Y. Kamide (1997), Statistical nature of geomagnetic storms, *J. Geophys. Res.*, *102*(A7), 14,215–14,222, doi:10.1029/97JA00903.

Zaharia, S., V. K. Jordanova, M. F. Thomsen, and G. D. Reeves (2008), Self-consistent geomagneticstorm simulation: The role of the induced electric fields, *J. Atmos. Solar-Terr. Phys.*, *70*.